doi:10.1038/nature13734

1. Gate dependence of the negatively charged trion in WS_2 monolayer.

We test the trion with both transport and optical measurements. The trion in our system is negatively charged, and is comprised of two electrons and one hole.

In our transport measurement, a field effect transistor (FET) is fabricated on a monolayer WS_2 using E-beam lithography. The substrate is a 285-nm SiO_2 layer on a heavily p doped silicon, allowing us to electrically tune the doping level of the WS_2 by applying the back gate voltage (V_{bg}). We apply a 0.1 V bias on the drain terminal, with the source terminal grounded. The contacting metal is Ti/Au (2/50 nm).

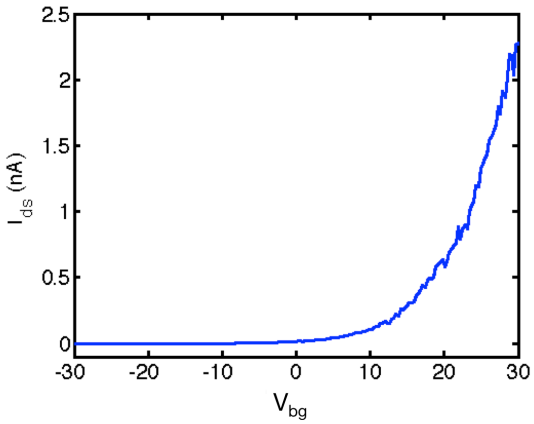

Fig. S1. Back gate voltage dependence of the source-drain current in a monolayer WS_2 based field effect transistor.

We measure the source-drain current as we sweep the V_{bg} (Fig. S1). Within our tuning range, no hole conduction can be observed. In the electron injection regime, the transistor is turned on at about 0 V. Therefore, our monolayer is electron doped if no back gate is applied, and the doping density is about 10^{11}-10^{12} cm^{-2}. As a result, a large portion of electron-hole pairs is bound to excessive electrons in the system, which leads to the emission of trions at 2 eV in additional to the exciton peak at 2.04 eV.

The exciton-trion picture is also directly confirmed by the doping dependent reflection spectrum. We measure the low temperature (10K) reflection spectra of the WS_2 monolayer on SiO_2/Si at different back gate voltages. (Fig. S2) Three sharp features can be observed corresponding to the 'A' (2.05), 'B' (2.45) and 'C' (2.82) excitons respectively. A and B features are highly sensitive to the doping level, as they involves the band edge states at K points, while the C exciton is insensitive to doping as it is related to the parallel bands near Γ point at higher energies[1]. The slow background in the relative reflectivity spectrum is induced by the red shift of the Fabry Perot resonance in the SiO_2 layer after the deposition of the monolayer.

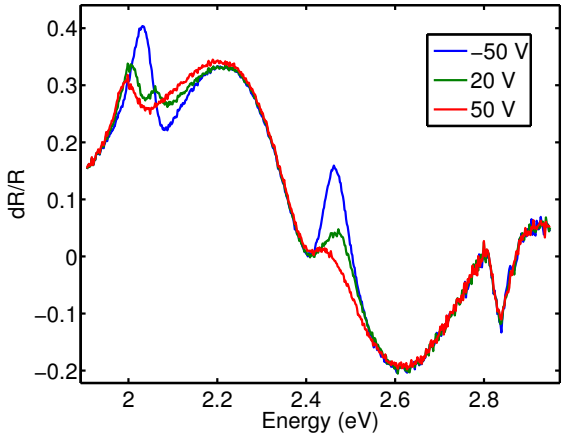

Fig. S2. Relative reflectivity spectra of a monolayer WS_2 on SiO_2/Si substrate at three different back gate voltages.

We closely examine the back gate voltage dependence of the A exciton reflectivity resonance. (Fig. S3) As the electron density increases, A exciton resonance decreases and splits at about 10V into two peaks, e.g. one exciton peak and one negatively charged trion peak, agreeing well with the FET threshold voltage. The splitting between the exciton and trion is about 40 meV at the onset, similar to the TPL emission spectrum. The trion peak experiences a red shift as the Fermi level is increased, indicating an increase in the trion binding energy, defined as the difference between trion and exciton level. The linear dependence of the trion binding energy on the monolayer doping level is originated from the band filling effect in the conduction band[2,3]. The natural electron doping in the monolayer at the zero back gate voltage can be introduced either by the impurity and defect in the as-grown crystal, or by the trapped charge on the substrate surface.

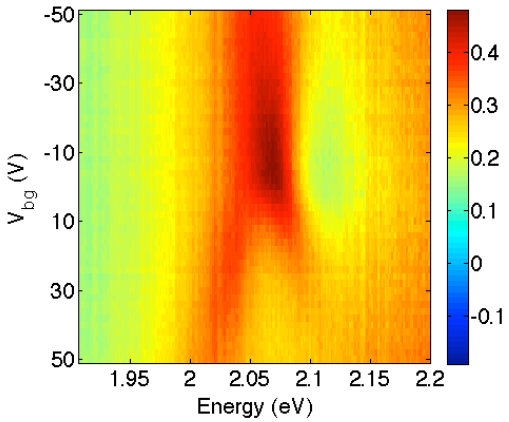

Fig. S3. Back gate voltage dependence of the 'A' exciton related reflectivity resonance.

2. Identification of exciton envelope function symmetry:

In our GW-BSE method, we first calculate the quasiparticle energies within the GW approximation. Then we use the Bethe-Salpeter equation (BSE) to solve for the two-particle electron-hole excitonic states, which have the form

$$|\Phi^s\rangle = \sum_k A_k^S |ck, vk\rangle \quad (1.)$$

where $|ck, vk\rangle$ denotes a free electron-hole pair configuration with the excited electron in the conduction band and the hole in the valence band at the k point of the Brillouin zone. We suppress the band indices in the summation, because the first few excited states in monolayer WS_2 only involve electron-hole configurations from the bottom conduction band and the top valence band. The exciton amplitude A_k^S is obtained by solving the BSE

$$(E_{ck} - E_{vk})A_k^S + \sum_{k'} \langle ck, vk|K^{eh}|ck', vk'\rangle A_{k'}^S = \Omega^s A_k^S \quad (2.)$$

where K^{eh} is the electron-hole interaction kernel. E_{ck} and E_{vk} corresponds to the quasiparticle energy of $|ck\rangle$ and $|vk\rangle$, respectively. Ω^s is the excitation energy of the excitonic state $|\Phi^s\rangle$. To calculate the oscillator strength and analyze the exciton symmetry, we write the wavefunction of the excitonic state $|\Phi^s\rangle$ in its real space representation

$$\Phi^s(\boldsymbol{r}_e, \boldsymbol{r}_h) = \sum_k A_k^S \varphi_{ck}(\boldsymbol{r}_e)\varphi_{vk}^*(\boldsymbol{r}_h) \quad (3.)$$

In agreement with a number of previous studies[4,5], we find that the valence band wavefunction φ_{vk} at the K valley has angular momentum $l = 0$, whereas the conduction band φ_{ck} has $l = \pm\hbar$ depending on the valley index. Therefore, the band-to-band transition is dipole allowed, and exhibits valley selective circular dichroism[6,7]. Also, the amplitude of the dipole matrix element of the band-to-band transition approaches a constant and finite value near the band edge.

The analyses of the exciton symmetry properties require the knowledge of the exciton amplitude A_k^S, whose real space representation (Fourier transformation) corresponds to the envelope function (hydrogenic-like orbital) of the exciton state S. To show the symmetry of the exciton amplitude A_k^S, we plot the 2D projected density of the exciton wavefunction with the position of the hole $\boldsymbol{r}_h$ fixed near a W atom (Fig.3b-f in the manuscript). Since $\boldsymbol{r}_h$ is fixed and the valence band wavefunction has angular momentum $l = 0$, these density plots represent the charge density of the electron atomic orbitals (each bright spot) modulated by real space exciton envelope function. In other words, these plots are faithful representations of the symmetry properties of the exciton amplitude A_k^S. As can be found in Fig.3b-f, the nodal characters along the radial direction are unique for each exciton state, and have a one to one correspondence with those of the 2D Rydberg series. Therefore, we may assign the hydrogen notations "1s", "2p", "2s", etc. to the individual exciton states.

Having identified the exciton envelope function symmetry for the series of states, we can further examine the optical oscillator strength for each exciton state. The oscillator strength for state S

$$F^S = \left| \sum_k \langle \psi_{ck}|\mathbf{e}\cdot\mathbf{v}|\psi_{vk}\rangle A_k^S \right|^2 \quad (4.)$$

is a convolution over the dipole-matrix element and the exciton amplitude. Since monolayer WS_2 is a dipole allowed material, the dipole-matrix elements are nonzero and nearly constant at the band edge. Therefore, the oscillator strength is only appreciable when the exciton amplitude A_k^S is nodeless, that

is the envelope function is s-like in real space, due to the coherent contribution from different k points. This is verified numerically in our calculations.

In our GW-BSE method, the wavefunctions φ_{vk} and φ_{ck} and the matrix elements of the electron-hole kernel, and hence A_k^S, are calculated consistently at each individual k point. Thus, the density plots of the real-space exciton wavefunction (Fig.3b-f) and the evaluation of the oscillator strengths are independent of the gauge choice, and therefore gauge invariant.

In this work, density functional calculations are performed using the local density approximation (LDA) implemented in the Quantum Espresso package [8]. The GW and GW+BSE calculations are performed with the BerkeleyGW package[9]. The dielectric matrix is constructed with a cutoff energy of 476 eV. The dielectric matrix and the self-energy are calculated on a 18x18x1 k-grid. The quasi-particle band gap is converged to within 0.05 eV. In the calculation of optical absorption spectra, the quasi-particle band structure and electron-hole interaction kernal are interpolated onto a 81x81x1 fine k-grid, with the 1s exciton binding energy converged to within 0.05 eV. The spin-orbit coupling is included perturbatively.

3. Two-photon excitation spectroscopy:

WS2 samples are directly exfoliated onto fused quartz substrates from a synthesized crystal (2d Semiconductors Inc.). The exfoliated monolayer flake is normally a few micrometers in size and characterized by tools including AFM, micro Raman and photoluminescence spectroscopy. The solid-state capping is 50 nm thick Al_2O_3, coated with the Atomic Layer Deposition (ALD) technique. The liquid capping is prepared by wetting the sample with deionized water or immersion oil (Zeiss, Immersol 518 F).

The two-photon excitation spectroscopy is carried out with an optical parametric oscillator (Newport, Inspire HF 100) pumped by a mode-locked Ti:sapphire oscillator. The laser pulse width is about 190 (±20) fs and repetition rate is 80 MHz. The low temperature experiment is operated in a continuous-flow liquid Helium cryostat equipped with a long working distance 50x objective of a 0.55 NA and the room temperature data is collected by a 100x objective of a 0.9 NA or a 1.4 NA 63x oil immersion objective. The emission signal is detected in the back scattering configuration and analyzed by a cooled CCD spectrometer. The transmissivity of the optical system is carefully calibrated to evaluate the absolute power level at the focal point. The emission spectra are normalized to the square of the focused power, as the excitation power is limited to the unsaturated regime. The laser pulse width is measured by a home-built autocorrelator at the focus throughout the scanning range. The micro reflectivity spectrum is measured with a focused supercontinuum laser (Fianium, SC450).

4. The exciton series deviation from the 2D hydrogen model

The energy series in 2D hydrogen can be expressed as $E_n = -me^4/(2(n-1/2)^2\hbar^2\varepsilon)$ [10], which indicates the energy ratio between 1*s*-2*p* and 1*s*-3*p* separations is 27/32. But as shown in fig. 2, our experimentally measured ratio, 6/11, is far from this value. More clearly, we compare the first-principles calculated excitonic levels and the predictions side by side. (Fig. S4)

Fig. S4. Left, energy levels of our theoretical results. Right, energy levels of the 2D hydrogen model.

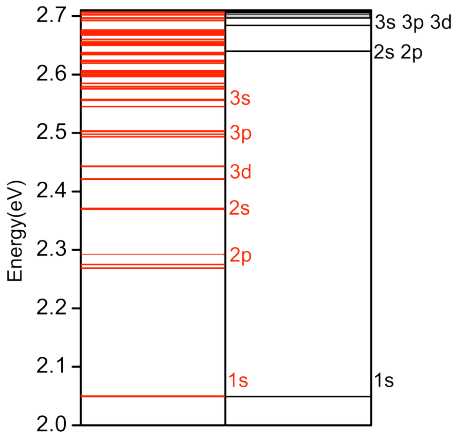

The 1s energy level and the quasiparticle band edge of the 2D hydrogen model are assumed to be the same as our theoretical results.

The labeling of the primary and orbital quantum number of each state is confirmed by checking the real space wavefunction of each exciton as plotted in fig. 3. Given the same total binding energy, the lower excited excitonic states are much lower in energy in our theoretical calculation. Such deviation was initially explored as the dielectric confinement effect by Keldysh in 1979[11]. Compared with Keldysh's analytical model, we don't limit the exciton wavefunction into certain regime in our first-principles calculations. Consequently, we are able to observe the non-degeneracy of the excitonic states with the same principle quantum number. Unlike the highly degenerate case in 2D hydrogen, the state of high angular momentum in the same shell is even lower in energy. (Fig. S4)

1. Kozawa, D. *et al.* Photocarrier relaxation in two-dimensional semiconductors. *arXiv* **1402,** 286 (2014).
2. Mak, K. F. *et al.* Tightly bound trions in monolayer MoS_2. *Nature Materials* **12,** 207–211 (2013).
3. Ross, J. S. *et al.* Electrical control of neutral and charged excitons in a monolayer semiconductor. *Nature Communications* **4,** (2013).
4. Xiao, D., Liu, G.-B., Feng, W., Xu, X. & Yao, W. Coupled Spin and Valley Physics in Monolayers of MoS_2 and Other Group-VI Dichalcogenides. *Phys. Rev. Lett.* **108,** 196802 (2012).
5. Cao, T. *et al.* Valley-selective circular dichroism of monolayer molybdenum disulphide. *Nature Communications* **3,** 887 (2012).
6. Mak, K. F., He, K., Shan, J. & Heinz, T. F. Control of valley polarization in monolayer MoS_2 by optical helicity. *Nature Nanotechnology* **7,** 494–498 (2012).
7. Zeng, H., Dai, J., Yao, W., Xiao, D. & Cui, X. Valley polarization in MoS_2 monolayers by optical pumping. *Nature Nanotechnology* **7,** 490–493 (2012).

8. Giannozzi, P. *et al.* QUANTUM ESPRESSO: a modular and open-source software project for quantum simulations of materials. *J Phys Condens Matter* **21,** 395502 (2009).
9. Deslippe, J. *et al.* BerkeleyGW: A massively parallel computer package for the calculation of the quasiparticle and optical properties of materials and nanostructures. *Computer Physics Communications* **183,** 1269–1289 (2012).
10. Yang, X., Guo, S., Chan, F., Wong, K. & Ching, W. Analytic solution of a two-dimensional hydrogen atom. I. Nonrelativistic theory. *Phys. Rev. A* **43,** 1186–1196 (1991).
11. Keldysh, L. V. Coulomb interaction in thin semiconductor and semimetal films. *Journal of Experimental and Theoretical Physics Letters* **29,** 658 (1979).